

# Cryogenic enhancement of phononic four-wave mixing in AlScN/SiC

A. K. Behera,<sup>1, a)</sup> B. Smith,<sup>2, a)</sup> X. Du,<sup>3</sup> Y. Deng,<sup>4</sup> M. Miller,<sup>2</sup> N. Sagartz,<sup>2</sup> M. Koppa,<sup>2</sup> C. T. Harris,<sup>1</sup> M. Lilly,<sup>1</sup> R. H. Olsson III,<sup>3</sup> M. Eichenfield,<sup>1,2,4</sup> and L. Hackett<sup>\*2</sup>

<sup>1)</sup>Center for Integrated Nanotechnologies, Sandia National Laboratories, Albuquerque, New Mexico 87185, USA

<sup>2)</sup>Microsystems Engineering, Science, and Applications, Sandia National Laboratories, Albuquerque, New Mexico 87123, USA

<sup>3)</sup>Department of Electrical and Systems Engineering, University of Pennsylvania, Philadelphia, Pennsylvania 19104, USA

<sup>4)</sup>Electrical, Computer and Energy Engineering, University of Colorado, Boulder, Colorado 80309, USA

(\*Electronic mail: lahacke@sandia.gov)

(Dated: 21 January 2026)

Surface acoustic wave platforms based on piezoelectric thin-film heterostructures provide sub-wavelength acoustic confinement, making them attractive for compact nonlinear phononic systems with applications including frequency conversion, parametric interactions, and nonlinear signal processing. Here, we investigate guided surface acoustic wave phononic four-wave mixing at gigahertz frequencies in an aluminum scandium nitride (Al<sub>0.58</sub>Sc<sub>0.42</sub>N)/4H–silicon carbide heterostructure operated at both room temperature (295 K) and cryogenic temperature (4 K). The 500 nm thick aluminum scandium nitride film supports guided Rayleigh and Sezawa modes with distinct displacement and strain energy density distributions, allowing a direct comparison of mode-dependent nonlinear behavior within the same device. Continuous-wave four-wave mixing measurements reveal an enhancement in the extracted modal nonlinear coefficient at 4 K relative to 295 K for both modes. In addition, the Rayleigh mode exhibits a modal nonlinearity approximately two orders of magnitude larger than that of the Sezawa mode across both temperature regimes. These results demonstrate that phononic four-wave mixing is strongly influenced by temperature, mode confinement, and strain localization while establishing aluminum scandium nitride on silicon carbide heterostructures as a promising platform for engineering enhanced nonlinear phononic interactions for future classical and quantum acoustic on-chip signal processing systems.

## I. INTRODUCTION

The optical Kerr effect, arising from a material’s third-order nonlinear susceptibility,  $\chi^{(3)}$ , has an acoustic analogue in which strain-dependent nonlinearities produce four-wave mixing between phonons.<sup>1–3</sup> In photonics, Kerr nonlinearities underpin a wide range of classical and quantum technologies, including wavelength conversion, frequency-comb generation, parametric amplification, and nonlinear quantum light generation.<sup>4–11</sup> Establishing mechanisms to harness and optimize on-chip phononic third-order nonlinear processes could bring similar functionality into the acoustic domain for classical radio frequency (RF) signal processing,<sup>12</sup> quantum phononics,<sup>13,14</sup> and hybrid quantum acoustic platforms that interface phonons with superconducting or solid-state quantum systems.<sup>15,16</sup>

Surface acoustic waves (SAWs) confine acoustic energy within approximately one wavelength of the surface, resulting in large local strain in a small effective mode volume.<sup>17,18</sup> In layered piezoelectric heterostructures, such as aluminum scandium nitride (AlScN) on silicon carbide (SiC), acoustic velocity mismatch between the thin film and substrate gives rise to guided slab-mode SAW phononic waveguides that exhibit enhanced vertical confinement over conventional SAWs. SAW-based technologies are becoming in-

creasingly diverse including acousto-optic beam steering,<sup>19</sup> biosensing,<sup>20</sup> microfluidics,<sup>21</sup> acoustic tweezers,<sup>22</sup> long-range exciton transport in two-dimensional materials,<sup>23</sup> and magnetoelastic modulation of magnetic domain walls<sup>24</sup> in addition to chip-scale components for the RF front end such as high performance filters,<sup>25</sup> amplifiers,<sup>26–28</sup> and oscillators.<sup>29–33</sup> Quantum SAW applications include manipulating superconducting qubit states,<sup>34,35</sup> performing spectroscopy and coherent operations on quantized phononic modes in nanomechanical resonators,<sup>36</sup> and enabling strain-mediated spin control.<sup>37</sup> Further understanding the mechanisms for harnessing nonlinearities in guided SAW modes provides a route to enhancing the functionality of existing SAW-based platforms, enabling integrated nonlinear phononic signal processors and new capabilities in hybrid quantum–acoustic interfaces, such as SAW-mediated coupling between phonons and co-integrated quantum systems. At the same time, a detailed understanding of phononic nonlinearities is essential for applications that demand highly linear operation, where suppressing unwanted nonlinear mixing is critical for preserving signal fidelity and quantum coherence.

On-chip phononic four-wave mixing has been previously demonstrated across several material platforms. A mechanical analogue of Kerr fiber optics was realized in a flexural-mode GaAs/AlGaAs nanoelectromechanical waveguide, where self-phase modulation, cross-phase modulation, and four-wave mixing were observed at megahertz frequencies.<sup>1</sup> Gigahertz-frequency four-wave mixing and cascaded sideband gener-

<sup>a)</sup>These authors contributed equally.

ation were shown in thin-film lithium niobate phononic integrated circuits.<sup>2</sup> In addition, electron-mediated phononic nonlinearities in semiconductor-piezoelectric heterostructures have been shown to significantly enhance the phononic third-order nonlinearity and thus the four-wave mixing power conversion efficiency compared to the case where the nonlinearity arises solely from the piezoelectric material.<sup>3,38</sup>

In this work, we study phononic four-wave mixing in a 500 nm thick aluminum scandium nitride/4H-silicon carbide ( $\text{Al}_{0.58}\text{Sc}_{0.42}\text{N}/\text{SiC}$ ) thin film heterostructure at gigahertz frequencies. We carry out four-wave-mixing measurements at room (295 K) and cryogenic (4 K) temperatures to characterize the intrinsic piezoelectric acoustic nonlinearity of the Rayleigh and Sezawa guided SAW modes supported in this material stack. The Rayleigh mode exhibits strongly surface-localized strain with coupled longitudinal (in-plane) and vertical (out-of-plane) displacements, whereas the Sezawa mode has a strain-energy profile that extends more deeply into the SiC substrate. Our results show a significant enhancement in four-wave mixing power conversion efficiency for the Rayleigh mode compared to the Sezawa mode, as well as a temperature-dependent enhancement for both modes at 4 K relative to 295 K.

To interpret these results, we apply the standard undepleted four-wave mixing model from Kerr nonlinear optics, which assumes linear loss and a power-independent modal nonlinear coefficient. Within this framework, the measured enhancement in conversion efficiency is consistent with an intrinsic increase in the modal nonlinearity. However, at the same time, our experimental results exhibit clear departures from the model's assumptions, revealing nonlinear behavior beyond that captured by a Kerr-type approximation. Overall, the results presented in this work offer additional insight into the nonlinear mechanisms governing guided SAW systems and establish new methods to engineer phononic devices that leverage controlled nonlinear interactions.

## II. EXPERIMENTAL PROCEDURES

The c-axis-oriented  $\text{Al}_{0.58}\text{Sc}_{0.42}\text{N}$  thin film was prepared on a 4H-SiC substrate by reactive pulsed-DC magnetron co-sputtering. The deposition was performed with a heater temperature of 500 °C and a  $\text{N}_2$  flow of 20 sccm. Magnetron powers of 875 W and 770 W were applied to the Al and the Sc targets, respectively. To suppress abnormally oriented grains, the AlScN stack was initiated with a 15 nm AlN seed layer followed by a 35 nm compositional gradient layer in which the Sc concentration was linearly increased from 0% to 42%.<sup>39,40</sup> A 450 nm thick layer of  $\text{Al}_{0.58}\text{Sc}_{0.42}\text{N}$  was then grown, such that the total piezoelectric film thickness was 500 nm.

The interdigital transducers (IDTs) of the piezoelectric acoustic wave delay line were fabricated on the  $\text{Al}_{0.58}\text{Sc}_{0.42}\text{N}/\text{SiC}$  platform using a two-step patterning process of electron beam (e-beam) lithography and photolithography. First, e-beam lithography defined the split finger IDT electrodes with an acoustic wavelength,  $\lambda$ , of 1.5  $\mu\text{m}$  followed by metal evaporation and liftoff of 5 nm titanium (Ti) and 70

nm aluminum (Al). A subsequent photolithography step patterned the bus lines connecting fingers of identical polarity to their contact pads for wirebonding. The sample was then loaded into an e-beam deposition chamber equipped with in-situ ion milling. A brief ion mill step removed any insulating  $\text{AlO}_x$  layer formed on the Al surface during ambient exposure, ensuring low-resistance electrical contact to a subsequent metal stack of 20 nm Ti and 200 nm gold (Au), which was evaporated onto the samples followed by liftoff to complete the fabrication.

The guided SAW delay line device used for four-wave mixing measurements was wirebonded to a Quantum Machines QBoard, which provides a low-loss, impedance-controlled RF interface compatible with cryogenic operation, and was measured in a custom Janis liquid-helium flow cryostat. Scattering parameters (S-parameters) of the guided SAW delay line devices were characterized using a calibrated Agilent Technologies E5071C vector network analyzer (VNA). For four-wave mixing experiments, two Keysight N5171B RF signal generators provided the pump tones, which were combined and applied to the input IDT. The output spectrum was characterized using an Agilent Technologies MXA N9020A signal analyzer with a 1 kHz resolution bandwidth and a 100 Hz video bandwidth. Propagation loss and acoustic reflectivity measurements were performed on separate test structures fabricated on a dedicated chip. Those measurements were carried out in a Montana Instruments cryostat using ground–signal–ground (GSG) RF probes.

## III. RESULTS AND DISCUSSION

Figure 1(a) shows the computed normalized displacement fields in the  $\text{Al}_{0.58}\text{Sc}_{0.42}\text{N}/\text{SiC}$  heterostructure for the Rayleigh and Sezawa modes at an acoustic wavelength of 1.5  $\mu\text{m}$  from a finite element method (FEM) model. The Rayleigh mode has a displacement amplitude that peaks at the free surface and then decreases with increasing depth into the SiC substrate. The majority of the strain energy density is confined within the  $\text{Al}_{0.58}\text{Sc}_{0.42}\text{N}$  layer. The associated particle motion is elliptical with mixed in-plane (longitudinal) and out-of-plane (vertical) displacement components, which leads to large in-plane and out-of-plane displacement gradients near the surface and a mixture of normal and shear strain components in the piezoelectric film. In contrast, the Sezawa mode exhibits mixed in-plane and out-of-plane particle motion that is distributed across the film thickness, with stronger participation near the  $\text{Al}_{0.58}\text{Sc}_{0.42}\text{N}/\text{SiC}$  interface. The displacement amplitude peaks within the  $\text{Al}_{0.58}\text{Sc}_{0.42}\text{N}$  layer, with a significantly larger fraction extending into the SiC substrate compared to the Rayleigh mode. The strain energy density is therefore more broadly distributed between the  $\text{Al}_{0.58}\text{Sc}_{0.42}\text{N}$  and the SiC.

We used FEM simulations to compute the acoustic eigenfrequencies of the Rayleigh and Sezawa modes with electrically open or shorted boundary conditions for a wavelength range of 1.3  $\mu\text{m}$  to 1.7  $\mu\text{m}$ . The resulting mode frequencies as a function of the acoustic propagation constant are shown

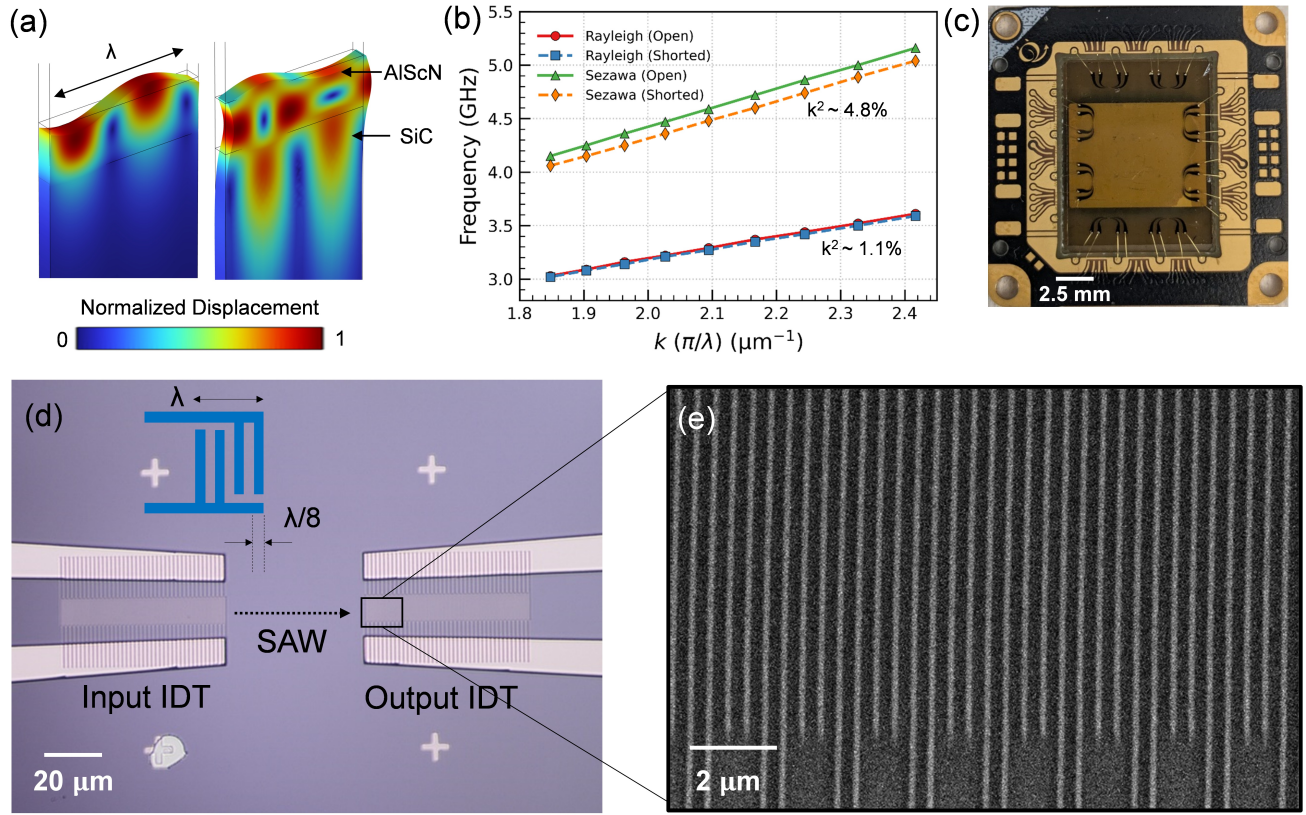


FIG. 1. (a) The modeled normalized mechanical displacement field for the Rayleigh mode (left) and Sezawa mode (right) in the 500 nm thick Al<sub>0.58</sub>Sc<sub>0.42</sub>N/SiC material platform. The acoustic wavelength,  $\lambda$ , was set to 1.5  $\mu\text{m}$ . (b) Modeled acoustic frequency with electrically open and shorted boundary conditions on the Al<sub>0.58</sub>Sc<sub>0.42</sub>N surface as a function of the acoustic propagation constant. The modeled  $k^2$  values for Rayleigh and Sezawa modes were 1.1% and 4.8%, respectively. (c) An image of the fabricated Al<sub>0.58</sub>Sc<sub>0.42</sub>N/SiC chip wirebonded onto a QBoard used for characterization. (d) A microscope image of a guided SAW delay line, which consists of an input IDT, a propagation region, and an output IDT. The inset shows a schematic of the split finger IDT design. (e) A scanning electron microscope image of the fabricated IDT electrodes.

in FIG. 1(b). As expected, we find that the Sezawa mode has a higher modeled electromechanical coupling coefficient,  $k^2$ , of  $\approx 4.8\%$  when compared to the Rayleigh mode, which has a modeled  $k^2$  value of  $\approx 1.1\%$ .

Figure 1(c) shows an optical image of a fabricated Al<sub>0.58</sub>Sc<sub>0.42</sub>N/SiC chip patterned with SAW delay lines wirebonded to a QBoard. Figure 1(d) shows a microscope image of a single delay line device that consists of input and output IDTs on the Al<sub>0.58</sub>Sc<sub>0.42</sub>N surface. The IDTs have a wavelength of 1.5  $\mu\text{m}$ , an aperture,  $A$ , of 10  $\mu\text{m}$ , and are separated by a propagation distance,  $L$ , of 50  $\mu\text{m}$ . The input IDT launches bi-directional SAWs by converting an applied RF electrical signal into a RF acoustic signal through the inverse piezoelectric effect. To suppress spurious reflections, we use a split finger IDT design in which each electrode with a width of  $\lambda/4$  is split into two electrodes with widths of  $\lambda/8$  spaced by  $\lambda/8$  (see inset FIG. 1(d)).<sup>18</sup> A scanning electron microscope image of the fabricated IDT electrodes with the split finger configuration is shown in FIG. 1(e).

We calibrated the VNA using a standard short-load-open-through (SLOT) method. VNA calibration removes the frequency-dependent effects of the measurement setup up to

the calibration plane, allowing isolated S-parameter measurements of the device under test. In our configuration, the calibration plane ended at the external connectors of the QBoard, such that the cryostat wiring and wirebonds were not calibrated out, which contributed to a broadband electromagnetic background in the measured S-parameter spectra.

The guided SAW delay line transmission,  $S_{21}$ , as a function of frequency is shown in FIG. 2(a) for 295 K and 4 K. Two transmission peaks appear at  $\approx 3.5$  GHz and  $\approx 4.7$  GHz, that we identify as the Rayleigh and Sezawa modes, respectively, from FEM modeling. A significant broadband electromagnetic background is present, which we attribute to the uncalibrated section of the measurement path.

From 295 K to 4 K, there is a transmission increase for both modes as well as a resonance frequency shift from 3.46 GHz to 3.48 GHz for the Rayleigh mode and 4.67 GHz to 4.7 GHz for the Sezawa mode. To isolate the piezoelectric acoustic contribution from the electromagnetic background, we performed a time-gating analysis. The measured complex  $S_{21}$  data was converted to the time domain using an Inverse Fast Fourier Transform (IFFT), a temporal window was applied around the expected acoustic arrival time, and the gated

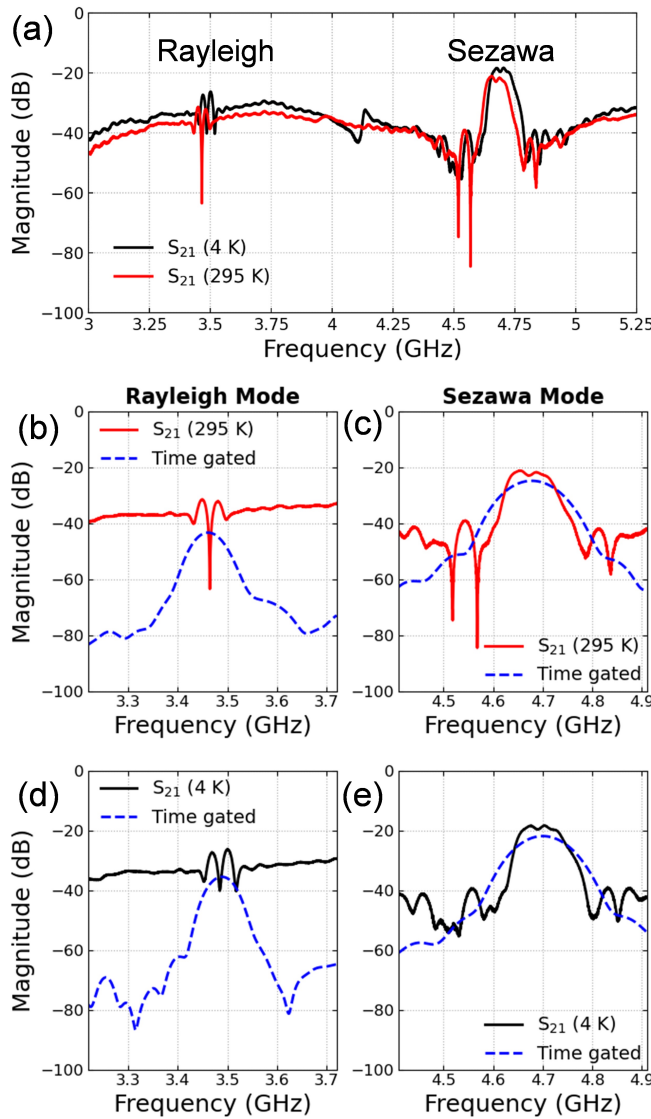


FIG. 2. (a)  $S_{21}$  as a function of frequency in the guided SAW delay line measured at 295 K and at 4 K. The local maxima across the transmission shows the Rayleigh and Sezawa modes at 3.5 GHz and at 4.7 GHz, respectively. (b,c) The measured transmission and the respective time gated transmission extracted for the delay line at 295 K for Rayleigh and Sezawa modes. (d,e) The measured transmission and the respective time gated transmission extracted for the delay line at 4 K for Rayleigh and Sezawa modes.

signal was then converted back to the frequency domain via a FFT to obtain the time-gated signal.

Figures 2 (b) and (c) show the measured and time-gated transmission for Rayleigh and Sezawa modes at 295 K, respectively. Figures 2(d) and (e) show the corresponding results at 4 K. At 295 K, the maximum measured transmission was -31.26 dB for the Rayleigh mode and -22.55 dB for the Sezawa mode, while at 4 K the transmission improved to -26.26 dB and -18.47 dB for the Rayleigh and Sezawa modes, respectively. The time-gated traces show similar trends, with increased transmission from -42.87 dB to -35.21 dB for the

Rayleigh mode and -24.71 dB to -21.62 dB for the Sezawa mode from 295 K to 4 K. The increased transmission at 4 K is consistent with a reduction in acoustic propagation loss in the  $\text{Al}_{0.58}\text{Sc}_{0.42}\text{N}/\text{SiC}$  heterostructure, likely arising from suppressed phonon-phonon scattering.

SAW four-wave mixing arises due to an effective third-order acoustic susceptibility,  $\chi_{\text{acoustic}}^{(3)}$ , that is expected to depend on factors such as strain localization, strain tensor symmetry, modal overlap with regions of large higher-order elastic and piezoelectric coefficients, nonlinear dielectric response, and interfacial effects. The differences in modal confinement and spatial field distribution for the Rayleigh and Sezawa modes makes the  $\text{Al}_{0.58}\text{Sc}_{0.42}\text{N}/\text{SiC}$  material platform compelling for investigating variations in nonlinear phononic behavior within the same device. When two phononic pump tones at angular frequencies  $\omega_1$  and  $\omega_2$  are launched into the delay line, degenerate four-wave mixing generates sidebands at  $\omega_{112} = 2\omega_1 - \omega_2$  and  $\omega_{221} = 2\omega_2 - \omega_1$ , as shown in the energy level diagrams in FIG. 3(a). The four-wave mixing measurement method utilized here is shown in FIG 3(b). Two RF signal generators supplied pump tones at frequencies  $f_1$  and  $f_2 = f_1 + \Delta f$  where  $\Delta f = 1$  MHz such that both pump tones remained within the IDT passbands for the Rayleigh and Sezawa modes, which were identified using the time-gated data for the transmission as a function of frequency. The pump tones were combined using a power combiner (PC) and then applied to the input IDT. As the acoustic waves propagated through the  $\text{Al}_{0.58}\text{Sc}_{0.42}\text{N}/\text{SiC}$  heterostructure, the third-order acoustic nonlinearity generated cascaded four-wave mixing sidebands, which were transduced back into electrical signals at the output IDT and recorded using a spectrum analyzer. For the first-order sidebands considered here, phase mismatch is negligible because the interaction region is short with an effective length,  $L_{\text{eff}}$ , of approximately 50  $\mu\text{m}$  and the acoustic dispersion over the relevant frequency span is weak. Using FEM-computed acoustic phase velocities to evaluate the wavevector mismatch,  $\Delta k$ , we find  $|\Delta k|L_{\text{eff}} \ll 1$ .

Figure 3(c) shows the measured four-wave mixing spectrum for the Rayleigh mode at 4 K. Two pump tones at  $f_1$  and  $f_2$  were centered at  $\approx 3.488$  GHz and the power on the RF signal generators was set to -10 dBm. Two distinct sidebands of lower amplitudes labeled as  $f_{112}$  and  $f_{221}$  appeared at a  $\Delta f$  frequency spacing away from  $f_1$  and  $f_2$ , respectively, which is consistent with degenerate four-wave mixing in the delay line. Figure 3(d) shows the corresponding spectrum for the Sezawa mode with the pump tones centered around  $\approx 4.702$  GHz. For the Rayleigh mode spectrum (FIG. 3 (c)), weaker secondary sidebands at  $2\Delta f$  were also present above the noise floor. For clarity, we label the primary pump tones as  $n = 0_-$  and  $0_+$  and the successive sidebands as  $n = \pm 1, \pm 2, \dots$ . The sideband power for a fixed length depends on the acoustic pump power, the acoustic propagation loss,  $\alpha$ , and the four-wave mixing modal nonlinear coefficient,  $\gamma_m$ , which parameterizes the strength of the underlying third-order acoustic nonlinearity.

The power conversion efficiency (PCE),  $\eta_{0\pm}$ , for degener-

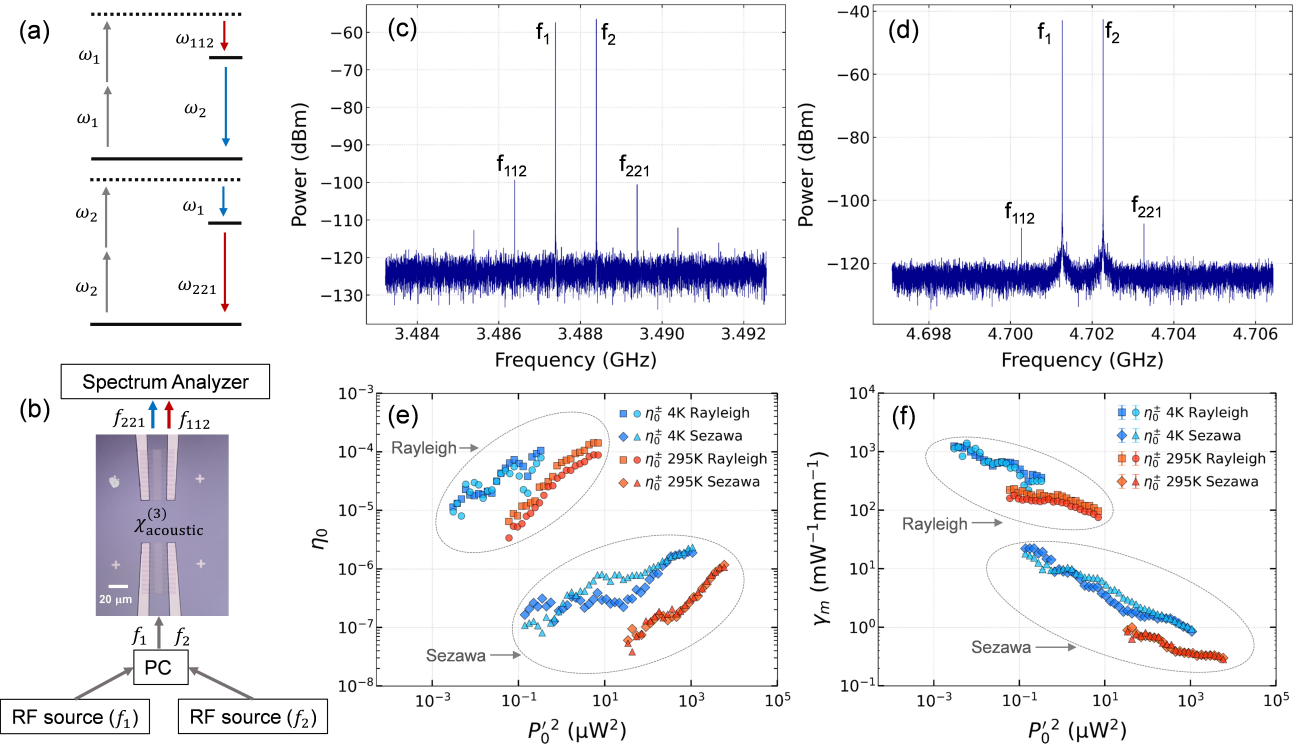


FIG. 3. (a) Energy-level diagrams illustrating degenerate four-wave mixing, where two phonons at one frequency and one phonon at a second frequency participate in a third-order acoustic nonlinear interaction via a  $\chi_{\text{acoustic}}^{(3)}$  to generate new sideband phonons. (b) A schematic of the the four-wave mixing experimental setup. Two RF sources were used to supply two pump tones to the input IDT driven at  $f_1$  and  $f_2$  frequencies. The output signal was collected by an IDT and characterized using a spectrum analyzer. (c,d) Comb lines observed due to four-wave mixing at 4 K for Rayleigh and Sezawa modes, respectively with the RF signal generator power set to -10 dBm. (e) Extracted power conversion efficiency,  $\eta_0$ , as a function of input acoustic pump power,  $P_0'^2$ , for the Rayleigh and Sezawa modes at 295 K and 4 K. (f) Extracted modal nonlinear coefficient,  $\gamma_m$ , as a function of input acoustic power,  $P_0'^2$ , at 295 K and 4 K.

ate four-wave mixing is given by

$$\eta_{0\pm} = \left| \frac{P_{1\mp}}{P_{0\pm}} \right| = \Gamma P_0'^2 \quad (1)$$

where  $P_{1\mp}$  is the measured sideband power,  $P_{0\pm}$  is the measured pump tone power,  $P_0'^2$  is the input acoustic pump power at the beginning of the SAW waveguide, and  $\Gamma$  is the four-wave mixing coefficient.  $P_0'^2$  was determined by first estimating the net loss across the measurement chain by calculating  $\text{Loss} = P_{\text{out}} - P_{\text{in}} - P_{\text{PC}}$  where  $P_{\text{out}}$  is the measured pump tone power,  $P_{\text{in}}$  is the RF signal generator power, and  $P_{\text{PC}}$  is the transmission of the power combiner, which was measured to be  $\approx -5.6$  dB over the frequency range of interest. Assuming symmetry of the experimental setup, the total loss, after subtracting propagation loss, was evenly divided between input and output losses which include contributions from cryostat cabling, wirebonds, and IDT transduction. This enables us to extract the acoustic pump power at the input IDT, which can be written as  $P_0' = P_{\text{in}} + P_{\text{PC}} + \frac{\text{Loss}}{2} - \frac{P_{\text{prop}}}{2}$  where  $P_{\text{prop}}$  is the propagation loss across the waveguide channel. The propagation losses were independently measured as discussed later in this section.

Figure 3(e) shows the extracted PCE for the Rayleigh and Sezawa modes at 295 K and 4 K on a log-log scale as a func-

tion of the squared input acoustic power. In the low power regime, we include only data for which the sideband powers are at least 4 dB above the spectral noise floor. At higher pump powers, we exclude data once the PCE clearly departs from the expected  $P_0'^2$  scaling, which is consistent with saturation or additional nonlinear processes.

Several trends emerge in the PCE depicted in FIG. 3 (e) as a function of  $P_0'^2$ . First, the PCE for both the Rayleigh and Sezawa modes increases with respect to  $P_0'^2$  at 295 K and 4 K, consistent with degenerate four-wave mixing. Second, two distinct groups of data emerge where the Rayleigh mode displays a significantly higher PCE compared to the Sezawa mode. Third, both modes display an enhanced PCE at 4 K compared to 295 K for a given input power. At 295 K, the maximum PCE for the Sezawa mode was  $1.5 \times 10^{-4}\%$  at an acoustic input power of  $78.2 \mu\text{W}$  whereas a significantly larger maximum PCE of  $1.7 \times 10^{-2}\%$  was achieved for the Rayleigh mode at a lower acoustic input power of  $2.63 \mu\text{W}$ . We calculated the four-wave mixing coefficient,  $\Gamma$ , from Eq. (1) by fitting the slope of measured PCE with respect to the input power. At 295 K,  $\Gamma = (1.9 \times 10^{-4} \pm 1.3 \times 10^{-5}) \text{ mW}^{-2}$  was obtained for the Sezawa mode, whereas a significantly larger value of  $\Gamma = (50.4 \pm 3.2) \text{ mW}^{-2}$  was extracted for the Rayleigh mode. Furthermore, we observed an enhancement

in the extracted four-wave mixing coefficient at 4 K as compared to 295 K where values of  $\Gamma = (3.9 \times 10^{-3} \pm 1.6 \times 10^{-4}) \text{ mW}^{-2}$  and  $\Gamma = (813 \pm 48) \text{ mW}^{-2}$  were obtained for Sezawa and Rayleigh modes at 4 K, respectively. The errors in the listed  $\Gamma$  values were obtained from the accuracy of the fits.

The modal nonlinear coefficient,  $\gamma_m$ , can then be calculated from the extracted  $\Gamma$  according to

$$\gamma_m = \frac{\sqrt{\Gamma}}{L_{\text{eff}}} \quad (2)$$

where  $L_{\text{eff}}$  is the effective nonlinear interaction length given by

$$L_{\text{eff}} = \left( \frac{1 - e^{-\alpha L}}{\alpha} \right) \quad (3)$$

where  $L$  is the physical length of the guided SAW waveguide and  $\alpha$  is the acoustic propagation loss. To estimate the acoustic propagation loss in the  $\text{Al}_{0.58}\text{Sc}_{0.42}\text{N}/\text{SiC}$  heterostructure, we fabricated multiple waveguides with identical split finger IDTs (FIG. 1 (d)) and varying propagation lengths ranging from 50  $\mu\text{m}$  to 500  $\mu\text{m}$  with a 50  $\mu\text{m}$  aperture. The 50  $\mu\text{m}$  aperture was used to suppress diffraction losses at longer propagation lengths. By measuring and fitting the peak transmission as a function of the propagation distance, we estimated the propagation loss for the Rayleigh and Sezawa modes at 295 K and 4 K. At 295 K, the extracted propagation losses were  $(106 \pm 19) \text{ dB/cm}$  for the Rayleigh mode and  $(96 \pm 8) \text{ dB/cm}$  for the Sezawa mode. After cooling to 4 K, the propagation losses were reduced to  $(8 \pm 40) \text{ dB/cm}$  and  $(24 \pm 8) \text{ dB/cm}$  for the Rayleigh and Sezawa modes, respectively. The substantially larger relative uncertainty for the Rayleigh mode at 4 K arises from the formation of a weak acoustic cavity due to reflections in the device, despite the use of a split finger IDT design, which is expected to significantly reduce the acoustic reflectivity of the transducer. By using the values for  $\alpha$  and  $\Gamma$  in Eq. (2) and Eq. (3), we determined the modal nonlinear coefficients. For the Rayleigh mode,  $\gamma_m = (151 \pm 9) \text{ mW}^{-1}\text{mm}^{-1}$  at 295 K and  $(573 \pm 22) \text{ mW}^{-1}\text{mm}^{-1}$  at 4 K were obtained. For the Sezawa mode, on the other hand, at 295 K,  $\gamma_m = (0.3 \pm 0.04) \text{ mW}^{-1}\text{mm}^{-1}$  was obtained with an enhancement to  $(1.3 \pm 0.2) \text{ mW}^{-1}\text{mm}^{-1}$  at 4 K. The errors in the reported  $\gamma_m$  originate from the relative errors in  $\Gamma$  and  $\alpha$ .

For the undepleted, Kerr-type model described by Eqs. (1) and (2), one would expect the modal nonlinear coefficient,  $\gamma_m$ , to be independent of input power. However, by investigating the extracted  $\gamma_m$  at each input power, we observe a clear power-dependent behavior. Figure 3(f) shows  $\gamma_m$  as a function of  $P_0^2$  for the Rayleigh and Sezawa modes at 295 K and 4 K extracted by using Eqs. (2) and (3). Just like the PCE, the data separates into two distinct groups corresponding to the Rayleigh and Sezawa modes, with the Rayleigh mode having a significantly larger  $\gamma_m$  as expected. At 295 K, the maximum values for  $\gamma_m$  were  $220 \text{ mW}^{-1}\text{mm}^{-1}$  for the Rayleigh mode and  $0.96 \text{ mW}^{-1}\text{mm}^{-1}$ . There is an enhancement to the  $\gamma_m$  values at 4 K when compared to 295 K. For the Rayleigh mode at 4 K, the maximum  $\gamma_m$  is  $1367 \text{ mW}^{-1}\text{mm}^{-1}$  while for the Sezawa mode at 4 K the maximum  $\gamma_m$  is  $22 \text{ mW}^{-1}\text{mm}^{-1}$ .

The experimentally observed power dependence and apparent reduction in  $\gamma_m$  with higher acoustic input power indicate that our results deviate from the simple Kerr-type description of four-wave mixing. At higher input power, additional nonlinear processes beyond degenerate four-wave mixing can become significant, including third-harmonic generation and higher-order mixing products that may divert acoustic power away from the measured four-wave mixing sidebands. These additional frequency components are strongly attenuated by the output IDT and therefore are not able to be captured in measured spectra. In addition, at large pump amplitudes, higher odd-order nonlinearities can generate cross-Kerr like sidebands at the same offest frequencies as those produced by the third-order process. Such contributions cannot be distinguished from  $\chi_{\text{acoustic}}^{(3)}$  driven sidebands in our measurements, yet they can exhibit substantially different pump-power scaling and relative sideband phases, which could contribute to the observed deviation from the simple Kerr model. As a result, extracting  $\gamma_m$  from only the four-wave mixing sideband power may not accurately capture the underlying  $\chi_{\text{acoustic}}^{(3)}$  at higher acoustic input power. An amplitude-dependent reduction of  $\chi_{\text{acoustic}}^{(3)}$ , which could arise from anharmonic elastic saturation, nonlinear dissipation, or mode-profile distortion at high strain, also cannot be excluded with only the data presented here.

We next examine factors that could influence the extracted modal nonlinear coefficients and potentially contribute to the observed differences between the Rayleigh and Sezawa modes. The undepleted, phase-matched four-wave mixing model applied here (Eqs. (1-3)), assumes single-pass acoustic propagation and neglects pump power enhancement that could arise from multiple reflections at the IDTs. Given the low propagation loss expected in a 50  $\mu\text{m}$  delay length, even small IDT reflections can lead to the formation of a weak acoustic cavity. Although the split finger IDT design utilized here (see Fig. 1(d)) is meant to reduce IDT reflectivity, small reflections over a short propagation distance combined with low propagation loss can still result in resonator pump power build-up within the guided SAW waveguide. In this case, the effective acoustic pump power participating in the nonlinear interaction can be enhanced relative to the assumed single-pass value.

We estimate the magnitude of the pump power enhancement using a resonant build-up factor:

$$B = \frac{1}{(1 - Re^{-\alpha L})^2} \quad (4)$$

where  $R$  is the IDT reflectivity. The intracavity pump power is then  $P_{0\pm}^{\text{cavity}} = BP_{0\pm}^{\prime}$ . Equation (4) assumes excitation on resonance and therefore provides an upper bound on the intracavity pump power enhancement and correspondingly on the cavity-induced modification of the modal nonlinearity. Here, we have treated the guided SAW waveguide as a phononic analogue of an optical Fabry-Perot cavity with internal resonance power enhancement with identical mirrors.<sup>41</sup>

We determined the reflectivity of our IDTs by characterizing the transmission ripples across the passband for both Rayleigh and Sezawa modes at 295 K and 4 K. The reflec-

tivity was determined according to  $R = \frac{1-\sqrt{1-V^2}}{V} e^{\alpha L}$ , where  $V = \frac{\sum_{i=1}^n (\frac{T_{max}-T_{min}}{T_{max}+T_{min}})}{n}$  is the fringe visibility calculated for  $n$  ripples where each ripple has a maximum and minimum transmission denoted by  $T_{max}$  and  $T_{min}$ , respectively.<sup>42</sup> We obtained reflectivities of 0.136 and 0.098 at 295 K for the Rayleigh and Sezawa modes, respectively. At 4 K, the reflectivity values increased to 0.3 for the Rayleigh mode and 0.135 for the Sezawa mode. Even with a substantial uncertainty in the propagation loss for Rayleigh mode at 4 K, the extracted reflectivity only changes by 10% because the propagation distance is short and therefore  $e^{\alpha L}$  is close to unity. The enhanced reflectivity that we extract at 4 K could be due to reduced resistive losses in the Al IDTs at cryogenic temperatures producing altered boundary conditions at the AlScN/Al interfaces.

To account for the pump power enhancement, the modal nonlinear coefficient was calculated according to

$$\gamma_m = \frac{\sqrt{\Gamma}}{BL_{\text{eff}}}. \quad (5)$$

According to Eq. 5, the Rayleigh mode four-wave mixing modal nonlinearity is  $(117 \pm 7) \text{ mW}^{-1} \text{ mm}^{-1}$  at 295 K and  $(283 \pm 11) \text{ mW}^{-1} \text{ mm}^{-1}$  at 4 K. The values for the Sezawa mode are  $(0.24 \pm 0.03) \text{ mW}^{-1} \text{ mm}^{-1}$  and  $(0.96 \pm 0.1) \text{ mW}^{-1} \text{ mm}^{-1}$  at 295 K and 4 K, respectively, with uncertainties originating from the four wave mixing coefficient,  $\Gamma$ , and propagation loss,  $\alpha$ , in  $B$  and  $L_{\text{eff}}$ . We therefore find that the cavity-enhanced pump power cannot account for the enhanced  $\gamma_m$  observed for the Rayleigh mode over the Sezawa mode and for 4 K compared to 295 K for both modes.

In addition to cavity effects, our  $\gamma_m$  values could also be impacted from undesirable nonlinear contributions in the measurement signal chain itself, such as a four-wave mixing nonlinearity arising from the power combiner or spectrum analyzer. To ensure that we only recorded the nonlinear properties of the guided SAW waveguide, we performed a control four-wave mixing measurement through the wirebonded QBoard bypassing our fabricated phononic waveguide. Under the spectrum analyzer settings used for this work, which were chosen specifically to lower the noise floor and also suppress analyzer-induced nonlinearities, we observed no sideband generation for the input powers reported in FIG. 3. Comb-like sidebands were only detected when the RF signal generator power exceeded the maximum values reported in this work by 25 dBm. This control experiment then confirmed that the measured four-wave mixing response that we report here is from the guided SAW waveguide.

#### IV. DISCUSSION

Previous experimental studies of on-chip phononic four-wave mixing at gigahertz frequencies have primarily focused on shear-horizontal or quasi-shear horizontal modes in lithium niobate thin film systems at room temperature.<sup>2,3</sup> To the best of our knowledge, here we report the first-ever gigahertz frequencies on-chip four-wave mixing for the Rayleigh and Sezawa modes and the first-ever measurements at cryogenic

temperatures. Our results suggest that the Rayleigh mode in the Al<sub>0.58</sub>Sc<sub>0.42</sub>N/SiC heterostructure supports an intrinsically large four-wave mixing modal nonlinear coefficient while the Sezawa mode may be more well-suited for applications where it is desirable to suppress the third-order nonlinearity. Furthermore, the spatial distributions of displacement fields and strain energy density play a critical role in determining nonlinear response. Guided structures that concentrate a large fraction of the strain energy density within the piezoelectric layer appear to be more favorable for strong nonlinear interactions. Incorporating lateral confinement into this material system via AlScN etching, which has already been demonstrated,<sup>43</sup> could provide a critical tool for engineering nonlinear overlap.

More broadly, the dependence of the intrinsic modal nonlinearity on waveguide width and effective mode area remains largely experimentally unexplored. In nonlinear optics, the modal nonlinear coefficients generally scale inversely with effective mode area, but the relationship is often more complex due to effects such as field redistribution and dispersion. A comparable, systematic understanding has not yet been established for phononic systems. The observed enhancement of phononic four-wave mixing at cryogenic temperatures does have direct analogues in nonlinear photonics, where Kerr-type nonlinear processes often exhibit increased efficiency at low temperatures due to reduced linear loss, suppression of thermally activated dissipation channels, and reduced nonlinear dissipation channels. Future work in phononic systems can leverage temperature-dependent measurements to assess the relative roles of intrinsic anharmonicity, nonlinear loss, and energy redistribution in cryogenic nonlinear acoustic interactions. It is also possible that the intrinsic phononic nonlinearity itself increases at cryogenic temperatures due to temperature-dependent higher-order elastic, piezoelectric, or dielectric coefficients, as well as modified defect and interfacial dynamics, leading to an enhanced effective nonlinear response.

Electron-mediated phononic nonlinearities also offer a route to enhance four-wave mixing.<sup>3</sup> An Al<sub>0.58</sub>Sc<sub>0.42</sub>N/SiC heterostructure has already been successfully integrated with a semiconductor thin film,<sup>39</sup> providing a clear path to study this method for enhancing phononic nonlinearities for the Rayleigh and Sezawa modes. Extending such approaches to cryogenically compatible and quantum platforms would require alternate semiconductor films with low carrier freeze-out, such as graphene.

Optimized and controllable phononic nonlinearities could open up new paths for hybrid acoustic quantum systems, including frequency conversion between disparate quantum modes, parametric amplification of mechanical excitations, and nonlinear phononic networks for signal routing and processing. In the classical domain, it is well-known that nonlinear phononic devices could enable compact mixers, correlators, and convolution engines with low power consumption. A more in-depth understanding of phononic nonlinearities is equally important for applications where nonlinear distortions can limit performance. Identifying the mechanisms that give rise to strong nonlinear interactions provides mechanisms for suppressing unwanted mixing, such as through mode selec-

tion, material modifications, or strain-distribution control.

## V. CONCLUSION

In this work, we have demonstrated phononic four-wave mixing in an  $\text{Al}_{0.58}\text{Sc}_{0.42}\text{N}/\text{SiC}$  heterostructure, investigating both Rayleigh and Sezawa guided SAW modes at room temperature (295 K) and cryogenic temperature (4 K). We found that the Rayleigh mode exhibits a substantially larger modal nonlinearity coefficient than the Sezawa mode, with an enhancement of approximately 450X at 4 K and 500X at 295 K. In addition, both modes show an increase in the four-wave mixing modal nonlinearity at 4 K relative to 295 K with an enhancement of approximately 4X for both Rayleigh and Sezawa modes.

These results highlight the strongly modal-dependent and temperature-dependent nature of phononic nonlinear interactions in guided SAW systems. The Rayleigh mode is highly surface-localized, with displacement and elastic strain energy concentrated within the AlScN thin film, whereas the Sezawa mode exhibits a more distributed field profile with significant elastic strain energy extending into the SiC substrate. The enhanced nonlinear response of the Rayleigh mode is therefore consistent with a larger proportion of the strain energy density within the film.

Overall, our findings demonstrate that displacement field distribution, elastic strain energy confinement, and operating temperature are critical parameters for enhancing or intentionally suppressing third-order nonlinear interactions in guided SAW platforms. These insights establish AlScN/SiC heterostructures as a promising and versatile testbed for engineering temperature-tunable phononic nonlinearities, with implications for both classical RF nonlinear signal processing and emerging quantum acoustic technologies operating at cryogenic temperatures.

## VI. ACKNOWLEDGMENTS

This work is supported by the Laboratory Directed Research and Development program at Sandia National Laboratories, a multimission laboratory managed and operated by National Technology and Engineering Solutions of Sandia LLC, a wholly owned subsidiary of Honeywell International Inc. for the US Department of Energy's National Nuclear Security Administration under contract DE-NA0003525. This work was performed, in part, at the Center for Integrated Nanotechnologies, an Office of Science User Facility, operated for the US Department of Energy Office of Science. This paper describes objective technical results and analysis. Any subjective views or opinions that might be expressed in the paper do not necessarily represent the views of the US Department of Energy or the US Government.

## VII. REFERENCES

- <sup>1</sup>M. Kurosu, D. Hatanaka, and H. Yamaguchi, "Mechanical Kerr Nonlinearity of Wave Propagation in an On-Chip Nanoelectromechanical Waveguide," *Phys. Rev. Appl.* **13**, 014056 (2020).
- <sup>2</sup>F. M. Mayor, W. Jiang, C. J. Sarabalis, T. P. McKenna, J. D. Witmer, and A. H. Safavi-Naeini, "Gigahertz Phononic Integrated Circuits on Thin-Film Lithium Niobate on Sapphire," *Phys. Rev. Appl.* **15**, 014039 (2021).
- <sup>3</sup>L. Hackett, M. Koppa, B. Smith, M. Miller, S. Santillan, S. Weatherred, S. Arterburn, T. A. Friedmann, N. Otterstrom, and M. Eichenfield, "Giant electron-mediated phononic nonlinearity in semiconductor-piezoelectric heterostructures," *Nat. Mater.* **23**, 1386–1393 (2024).
- <sup>4</sup>G. Lin and Q. Song, "Kerr Frequency Comb Interaction with Raman, Brillouin, and Second Order Nonlinear Effects," *Laser & Photonics Reviews* **16**, 2100184 (2022).
- <sup>5</sup>J. R. Stone, X. Lu, G. Moille, D. Westly, T. Rahman, and K. Srinivasan, "Wavelength-accurate nonlinear conversion through wavenumber selectivity in photonic crystal resonators," *Nat. Photon.* **18**, 192–199 (2024).
- <sup>6</sup>S. Miller, K. Luke, Y. Okawachi, J. Cardenas, A. L. Gaeta, and M. Lipson, "On-chip frequency comb generation at visible wavelengths via simultaneous second- and third-order optical nonlinearities," *Opt. Express, OE* **22**, 26517–26525 (2014).
- <sup>7</sup>T.-H. Wu, L. Ledezma, C. Fredrick, P. Sekhar, R. Sekine, Q. Guo, R. M. Briggs, A. Marandi, and S. A. Diddams, "Visible-to-ultraviolet frequency comb generation in lithium niobate nanophotonic waveguides," *Nat. Photon.* **18**, 218–223 (2024).
- <sup>8</sup>N. Kuznetsov, A. Nardi, J. Riemsberger, A. Davydova, M. Churaev, P. Seidler, and T. J. Kippenberg, "An ultra-broadband photonic-chip-based parametric amplifier," *Nature* **639**, 928–934 (2025).
- <sup>9</sup>G. Moody, L. Chang, T. J. Steiner, and J. E. Bowers, "Chip-scale nonlinear photonics for quantum light generation," *AVS Quantum Sci.* **2**, 041702 (2020).
- <sup>10</sup>O. Yesharim, I. Hurvitz, J. Foley-Comer, and A. Arie, "Bulk nonlinear metamaterials for generation of quantum light," *Appl. Phys. Rev.* **12**, 011323 (2025).
- <sup>11</sup>O. Tziperman, G. Baranes, A. Gorlach, R. Ruimy, C. Mechel, M. Faran, N. Gutman, A. Pizzi, and I. Kaminer, "Nonlinear Quantum Light Generation in Collective Spontaneous Emission," *ACS Nano* **19**, 21260–21270 (2025).
- <sup>12</sup>C. Campbell, *Surface acoustic wave devices and their signal processing applications* (Elsevier, 2012).
- <sup>13</sup>E. Dumur, K. Satzinger, G. Peairs, M.-H. Chou, A. Bienfait, H.-S. Chang, C. Conner, J. Grebel, R. Povey, Y. Zhong, and others, "Quantum communication with itinerant surface acoustic wave phonons," *npj Quantum Information* **7**, 173 (2021).
- <sup>14</sup>M.-H. Chou, H. Qiao, H. Yan, G. Andersson, C. R. Conner, J. Grebel, Y. J. Joshi, J. M. Miller, R. G. Povey, X. Wu, and others, "Deterministic multi-phonon entanglement between two mechanical resonators on separate substrates," *Nature Communications* **16**, 1450 (2025).
- <sup>15</sup>A. Clerk, K. Lehnert, P. Bertet, J. Petta, and Y. Nakamura, "Hybrid quantum systems with circuit quantum electrodynamics," *Nature Physics* **16**, 257–267 (2020).
- <sup>16</sup>M. V. Gustafsson, T. Aref, A. F. Kockum, M. K. Ekström, G. Johansson, and P. Delsing, "Propagating phonons coupled to an artificial atom," *Science* **346**, 207–211 (2014).
- <sup>17</sup>C. Campbell, *Surface Acoustic Wave Devices for Mobile and Wireless Communications, Four-Volume Set* (Academic Press, 1998).
- <sup>18</sup>D. ROYER and E. Dieulesaint, *Elastic Waves in Solids I: Free and Guided Propagation* (Springer Science & Business Media, 1999).
- <sup>19</sup>B. Li, Q. Lin, and M. Li, "Frequency-angular resolving LiDAR using chip-scale acousto-optic beam steering," *Nature* **620**, 316–322 (2023).
- <sup>20</sup>K. Länge, B. E. Rapp, and M. Rapp, "Surface acoustic wave biosensors: a review," *Anal Bioanal Chem* **391**, 1509–1519 (2008).
- <sup>21</sup>X. Ding, P. Li, S.-C. Steven Lin, Z. S. Stratton, N. Nama, F. Guo, D. Slotcavage, X. Mao, J. Shi, F. Costanzo, and T. Jun Huang, "Surface acoustic wave microfluidics," *Lab on a Chip* **13**, 3626–3649 (2013).
- <sup>22</sup>A. Ozcelik, J. Rufo, F. Guo, Y. Gu, P. Li, J. Lata, and T. J. Huang, "Acoustic tweezers for the life sciences," *Nat Methods* **15**, 1021–1028 (2018).

<sup>23</sup>R. Peng, A. Ripin, Y. Ye, J. Zhu, C. Wu, S. Lee, H. Li, T. Taniguchi, K. Watanabe, T. Cao, X. Xu, and M. Li, “Long-range transport of 2D excitons with acoustic waves,” *Nat Commun* **13**, 1334 (2022).

<sup>24</sup>D. Froes, M. Arana, J. P. Sinnecker, and L. C. Sampaio, “Magnetoelastic modes in Néel domain walls,” *J. Appl. Phys.* **132**, 223908 (2022).

<sup>25</sup>R. Lu, “Recent advances in high-performance millimeter-Wave acoustic resonators and filters using thin-film lithium niobate,” *Progress in Quantum Electronics* **100-101**, 100565 (2025).

<sup>26</sup>H. Mansoorzare and R. Abdolvand, “Micromachined heterostructured lamb mode waveguides for acoustoelectric signal processing,” *IEEE Transactions on Microwave Theory and Techniques* **70**, 5195–5204 (2022).

<sup>27</sup>L. Hackett, M. Miller, S. Weatherred, S. Arterburn, M. J. Storey, G. Peake, D. Dominguez, P. S. Finnegan, T. A. Friedmann, and M. Eichenfield, “Non-reciprocal acoustoelectric microwave amplifiers with net gain and low noise in continuous operation,” *Nat Electron* **6**, 76–85 (2023).

<sup>28</sup>S. Ghosh, M. A. Hollis, and R. J. Molnar, “Acoustoelectric amplification of Rayleigh waves in low sheet density AlGaN/GaN heterostructures on sapphire,” *Appl. Phys. Lett.* **114**, 063502 (2019).

<sup>29</sup>C.-Y. Chang, Y.-C. Yu, Z.-Q. Lee, and M.-H. Li, “A Voltage-Controlled Surface Acoustic Wave Oscillator Based on Lithium Niobate on Sapphire Low-Loss Acoustic Delay Line,” *IEEE Transactions on Ultrasonics, Ferroelectrics, and Frequency Control* **71**, 1314–1323 (2024).

<sup>30</sup>S. Zhang, R. Lu, H. Zhou, S. Link, Y. Yang, Z. Li, K. Huang, X. Ou, and S. Gong, “Surface Acoustic Wave Devices Using Lithium Niobate on Silicon Carbide,” *IEEE Transactions on Microwave Theory and Techniques* **68**, 3653–3666 (2020).

<sup>31</sup>S. Tanaka, K. Park, and M. Esashi, “Lithium-niobate-based surface acoustic wave oscillator directly integrated with CMOS sustaining amplifier,” *IEEE Transactions on Ultrasonics, Ferroelectrics, and Frequency Control* **59**, 1800–1805 (2012).

<sup>32</sup>Z. Xi, J. G. Thomas, J. Ji, D. Wang, Z. Cen, I. I. Kravchenko, B. R. Srijanto, Y. Yao, Y. Zhu, and L. Shao, “Low-phase-noise surface-acoustic-wave oscillator using an edge mode of a phononic band gap,” *Physical Review Applied* **23**, 024054 (2025).

<sup>33</sup>A. Wendt, M. J. Storey, M. Miller, D. Anderson, E. Chatterjee, W. Horrocks, B. Smith, L. Hackett, and M. Eichenfield, “An Electrically Injected and Solid State Surface Acoustic Wave Phonon Laser,” arXiv preprint arXiv:2505.14385 (2025).

<sup>34</sup>J.-M. Pirkkalainen, S. U. Cho, J. Li, G. S. Paraoanu, P. J. Hakonen, and M. A. Sillanpää, “Hybrid circuit cavity quantum electrodynamics with a micromechanical resonator,” *Nature* **494**, 211–215 (2013).

<sup>35</sup>S. Maity, L. Shao, S. Bogdanović, S. Meesala, Y.-I. Sohn, N. Sinclair, B. Pingault, M. Chalupnik, C. Chia, L. Zheng, K. Lai, and M. Lončar, “Coherent acoustic control of a single silicon vacancy spin in diamond,” *Nat Commun* **11**, 193 (2020).

<sup>36</sup>P. Arrangoiz-Arriola, E. A. Wollack, Z. Wang, M. Pechal, W. Jiang, T. P. McKenna, J. D. Witmer, R. Van Laer, and A. H. Safavi-Naeini, “Resolving the energy levels of a nanomechanical oscillator,” *Nature* **571**, 537–540 (2019).

<sup>37</sup>S. Maity, B. Pingault, G. Joe, M. Chalupnik, D. Assumpção, E. Cornell, L. Shao, and M. Lončar, “Mechanical Control of a Single Nuclear Spin,” *Phys. Rev. X* **12**, 011056 (2022).

<sup>38</sup>H. Mansoorzare and R. Abdolvand, “Acoustoelectric-driven frequency mixing in micromachined lithium niobate on silicon waveguides,” in *2023 IEEE 36th International Conference on Micro Electro Mechanical Systems (MEMS)* (IEEE, 2023) pp. 1183–1185.

<sup>39</sup>L. Hackett, X. Du, M. Miller, B. Smith, S. Santillan, J. Montoya, R. Reyna, S. Arterburn, S. Weatherred, T. Friedmann, and others, “S-band acoustoelectric amplifier in an InGaAs-AlScN-SiC architecture,” *Applied Physics Letters* **124** (2024).

<sup>40</sup>X. Du, N. Sharma, Z. Tang, C. Leblanc, D. Jariwala, and R. H. Olsson, “Near 6-GHz Sezawa Mode Surface Acoustic Wave Resonators Using AlScN on SiC,” *Journal of Microelectromechanical Systems* **33**, 577–585 (2024).

<sup>41</sup>R. W. Boyd, *Nonlinear Optics* (Elsevier, 2008).

<sup>42</sup>F. L. Pedrotti, L. M. Pedrotti, and L. S. Pedrotti, *Introduction to Optics* (Cambridge University Press, 2017).

<sup>43</sup>Y. Deng, D. Anderson, X. Du, W. Roberts, M. Miller, B. Smith, L. Hackett, R. H. Olsson, and M. Eichenfield, “Monolithic AlScN/SiC phononic waveguides for scalable acoustoelectric and quantum devices,” *APL Materials* **13** (2025).